HHS Public Access

Author manuscript

Circ Cardiovasc Imaging. Author manuscript; available in PMC 2020 July 12.

Published in final edited form as:

Circ Cardiovasc Imaging. 2019 July ; 12(7): e009063. doi:10.1161/CIRCIMAGING.119.009063.

Non-invasive *in vivo* quantification of AAV9-mediated expression of the sodium/iodide Symporter (NIS) under hind-limb ischemia and neuraminidase desialylation in skeletal muscle using SPECT/CT

Nabil E. Boutagy, PhD[a,#], **Silvia Ravera, PhD**[b,#], **Xenophon Papademetris, PhD**[c], **John A. Onofrey, PhD**[c], **Zhen W. Zhuang, MD**[a], **Jing Wu, PhD**[c], **Attila Feher, MD, PhD**[a], **Mitchel R. Stacy, PhD**[a], **Brent A. French, PhD**[d,e], **Brian H. Annex, MD**[d,e], **Nancy Carrasco, MD**[b], and **Albert J. Sinusas, MD**[a,c]

[a.] Section of Cardiovascular Medicine, Department of Medicine, Yale Translational Research Imaging Center, Yale School of Medicine, New Haven, CT 06520, USA

[b.] Department of Cellular and Molecular Physiology, Yale School of Medicine, New Haven, CT 06510, USA

[c.] Department of Radiology and Biomedical Imaging, Yale School of Medicine, New Haven, CT 06520, USA

[d.] Department of Biomedical Engineering, University of Virginia, Charlottesville, VA, USA

[e.] Division of Cardiovascular Medicine/Department of Medicine, University of Virginia, Charlottesville, VA 22908, USA.

Abstract

Background—We propose microSPECT/CT imaging of the human sodium/iodide symporter (hNIS) to noninvasively quantify AAV9-mediated gene expression in a murine model of peripheral artery disease (PAD).

Methods—AAV9-hNIS ($2 * 10^{11}$ vpg) was injected into non-ischemic or ischemic gastrocnemius (GA) muscles of C57Bl/6J mice following unilateral hind-limb ischemia (HLI) ± the α-sialidase neuraminidase (NA). Control non-ischemic limbs were injected with phosphate buffer saline (PBS) or remained non-injected. Twelve mice underwent microSPECT/CT imaging after serial injection of $^{99m}TcO_4^-$, a NIS substrate, up to 28 days after AAV9-hNIS injection. Twenty-four animals were euthanized at selected times over one month for *ex vivo* validation. Forty-two animals were imaged with $^{99m}TcO_4^-$ ± the selective NIS inhibitor perchlorate (ClO_4^-) on day 10, to ascertain specificity of radiotracer uptake. Tissue was harvested for *ex vivo* validation. A modified version of the U-Net deep learning algorithm was used for image quantification.

Address for Correspondence: Albert J. Sinusas, MD, FACC, Section of Cardiovascular Medicine, Yale University School of Medicine, P.O. Box 208017, Dana 3, New Haven, CT 06520-8017, Tel: 203-785-5005, Fax: 203-737-1026.

[#]Denotes that both authors contributed equally to this work.

Disclosures:

XP consults for Brain Electrophysiology Laboratory Company (BELCO).

Results—As quantitated by standardized uptake value (SUV), there was a gradual temporal increase in $^{99m}TcO_4^-$ uptake in muscles treated with AAV9-hNIS. HLI, NA and HLI plus NA increased the magnitude of $^{99m}TcO_4^-$ uptake by 4–5 fold compared to non-ischemic muscle treated with only AAV9-hNIS. ClO_4^- treatment significantly reduced $^{99m}TcO_4^-$ uptake in AAV9-hNIS-treated muscles, demonstrating uptake specificity. The imaging results correlated well with *ex vivo* well counting (r^2=0.9375, P<0.0001) and immunoblot analysis of NIS protein (r^2=0.65, P<0.0001).

Conclusions—MicroSPECT/CT imaging of hNIS-mediated $^{99m}TcO_4^-$ uptake allows for accurate *in vivo* quantification of AAV9-driven gene expression, which increases under ischemic conditions or neuraminidase desialylation in skeletal muscle.

Keywords

Single Photon Emission Computed Tomography (SPECT); Adeno-associated virus 9 (AAV9); Sodium/Iodide Symporter (NIS); Peripheral Artery Disease (PAD)

Journal Subject Terms

Animal Models of Human Disease; Gene Therapy; Translational Studies

Introduction

Peripheral artery disease (PAD) is defined as atherosclerosis in arteries other than the coronary and intracranial vessels, but it most commonly affects vessels in the lower extremities [1]. Approximately 8.5 million Americans over the age of 40 have PAD, with an age-dependent prevalence that affects up to 20% of the population over the age of 80 [2]. In its severe form, PAD patients may experience leg pain at rest and/or develop non-healing foot ulcers, which is defined as critical limb ischemia (CLI). About a third of patients with CLI undergo major amputation, and are at a high risk of death from cerebrovascular, cardiovascular and all-cause events [1]. Although managing PAD patients with antiplatelet, antihypertensive and cholesterol-lowering medications reduces the risk of cardiovascular and cerebrovascular events, these medications do not significantly lower the risk of major lower extremity amputation [1].

Novel therapeutic approaches, such as gene delivery of angiogenic factors that stimulate the growth of new blood vessels in ischemic tissues, have been investigated using several delivery systems and therapeutic genes [3, 4]. A number of pre-clinical studies have demonstrated that AAV-mediated gene therapy provides improved recovery from surgically-induced hind-limb ischemia (HLI) [5, 6]. However, despite the promise of pre-clinical studies using AAV or other vector systems, the majority of clinical trials applying/using gene therapy in patients with PAD have been largely unsuccessful [3, 4]. Some explanations for the inability to translate effective angiogenic gene therapy from pre-clinical models to PAD patients include vector-related host immunogenic responses and the use of vectors that are expressed only for a short time and inadequate scaling up of the vector dose from animals to humans, leading to sub-optimal distribution, duration and magnitude of therapeutic gene expression.

The use of adeno-associated virus (AAV)–based vectors, which have low immunogenicity and provide for long term gene expression in muscle tissue has addressed some of the limitations in previous gene therapy clinical trials [7]. Other novel strategies, such as the selection of viral vector serotypes that have tissue-specific tropisms, as well as bio-engineered viral vectors to increase tissue-targeted vector delivery and therapeutic gene expression, have also been investigated [8, 9]. Along these lines, it has been shown that AAV serotype 9 transduction to striated muscle is superior to other AAV serotypes [10], and that AAV9 more efficiently targets ischemic than non-ischemic skeletal muscle [8]. In an attempt to increase AAV9 gene expression, the α-sialidase neuraminidase (NA) from *Vibrio cholera* type II, which exposes the primary receptor (terminal *N*-linked ß-galactose residues) of AAV9, has been used as an adjuvant to increase AAV9 gene expression in non-ischemic murine skeletal muscle [11].

As novel techniques are developed to optimize gene therapy, the ability to non-invasively track the spatial biodistribution, magnitude and persistence of viral-gene expression *in vivo* is necessary to assess the efficacy of gene transfer at both the preclinical and clinical levels. In the above-mentioned preclinical studies, serial *in vivo* monitoring of AAV9 gene expression was monitored semi-quantitatively using fluorescent reporter probes and bioluminescence imaging [9–12]. Although useful for tracking gene delivery in small animal applications, accurate quantification of gene delivery is limited by tissue depth and photon attenuation, which make these techniques non-translatable to large animal models and humans[12].

The sodium/iodide symporter (NIS), a member of solute carrier family 5 (SLC5), is the key plasma membrane protein that mediates active iodide (I^-) uptake in the thyroid gland [13]. NIS utilizes the Na^+ gradient generated by the Na^+/K^+ ATPase as its driving force, coupling the transport of 2 Na^+ to that of each I^-. NIS transports many radioisotopes, such as pertechnetate ($^{99m}TcO_4^-$), perrhenate ($^{186,188}ReO_4^-$), $^{123,124,131}I$, and [^{18}F]-tetrafluoroborate, and thus has been widely used as an *in vivo* reporter probe for imaging in many pre-clinical applications and in several phase I and phase II clinical trials of gene therapy [14]. NIS provides a method to non-invasively track vector gene expression using single photon emission computed tomography (SPECT) or positron emission tomography (PET) imaging, in combination with anatomical computed tomography (CT) imaging [14]. More recently, NIS made it possible to serially evaluate several novel strategies for delivering AAV9 to the myocardium of adult canines using SPECT/CT [15]. However, to our knowledge, the spatial distribution and magnitude of AAV9-mediated gene expression have yet to be investigated in non-ischemic and ischemic skeletal muscle using NIS and SPECT/CT. Therefore, we hypothesized that the use of human (h) NIS as a reporter gene for AAV9-mediated transduction would allow for non-invasive *in vivo* evaluation of the spatiotemporal distribution of AAV9-mediated transgene expression in skeletal muscle using microSPECT/CT in a mouse model of PAD and following NA-mediated desialylation.

Materials and Methods

The data that support the findings of this study are available from A.J.S. upon request.

Experimental Design

Male C57BL/6J mice (10–15 weeks old, n=78) were purchased from the Jackson Laboratory (Bar Harbor, ME). All animals were used in accordance with protocols and policies approved by the Yale Institutional Animal Care and Use Committee. Animals were separated into two groups that allowed for a) *in vivo* specificity of hNIS-mediated $^{99m}TcO_4^-$ uptake (n = 42), and b) serial assessment of hNIS expression over 28 days (n = 36) as described in detail in the supplemental materials and illustrated in Figure 1.

Animal Procedures

Unilateral Hind-limb Ischemia Surgery—Forty-eight mice underwent surgical occlusion of the right femoral artery to induce unilateral HLI according to the procedure previously reported [16, 17] and described in more detail in the supplemental materials. Notably, this ligation site induces ischemia in musculature of distal hind-limb, particularity in the distal hamstring, gastrocnemius (GA) and soleus muscles [17].

AAV9 vector and Neuraminidase delivery—The AAV9 vector system used incorporates a cytomegalovirus (CMV) promoter driving the expression of hNIS linked to eGFP via an IRES element (AAV9 pzac2.1-CMV-NIS-IRES-eGFP [AAV9-hNIS]. The AAV9 vectors were packaged by ViGene Biosciences (Rockville, MD) and delivered intramuscularly ($2*10^{11}$ viral genome particles [vgp]) into the GA muscle with a 31-gauge insulin needle as described in the supplemental materials. In addition, in a subgroup of mice, NA from *Vibrio cholera* type II (0.010 units) was mixed with AAV9-hNIS ($2*10^{11}$ vpg) and was injected into ischemic or non-ischemic muscle. Controls limbs were injected in an identical fashion to vector injections with a matched volume of phosphate buffered saline (PBS).

MicroSPECT/CT Imaging—Imaging was performed under light isoflurane anesthesia (1.5–2.0%). At all imaging sessions, mice were injected retro-orbitally with ~1 mCi of $^{99m}TcO_4^- \pm ClO_4^-$ (4 mg). Ninety minutes following tracer injection, microSPECT images of the hind-limbs were acquired for 15 minutes in list-mode on a hybrid multi-pinhole SPECT/CT camera (U-SPECT^{4}CT, MI Labs, Utrecht, Netherlands) with an ultra-high detection sensitivity (>13000 cps/MBq) and high resolution (0.85 mm) collimator using system software (version V6.21). On day 10, a subgroup of mice (n=15) underwent full-body microSPECT imaging for 30 minutes in list-mode following hind-limb imaging. Following SPECT imaging, all animals underwent a non-contrast microCT (50 KeV, 36 uA) to facilitate volume of interest (VOI) placement on the GA for image analysis.

MicroSPECT/CT Image Reconstruction—List mode data were reconstructed using the photopeak of ^{99m}Tc (126 – 154 keV) along with background windows below (120.4 – 126 keV) and above (154.0 – 159.6 keV) the photopeak for scatter and background correction. SPECT imaging was reconstructed using ordered subset expectation maximization (OS-EM), while CT images were reconstructed using the filtered back-projection algorithm using system reconstruction software (version V3.26) as described in the supplemental materials.

MicroSPECT/CT Image Analysis—We trained a deep neural network to perform segmentation of the VOIs of the left and right GA muscles on microCT images (Figure 2) using a modified version of the U-Net [18] fully-convolutional encoding-decoding architecture as described in detail in the supplemental materials.

$^{99m}TcO_4^-$ retention on microSPECT images was then quantified by applying the generated VOIs onto the microSPECT images, which were registered to microCT images, to derive mean image count activity in mCi/cc using in house software (BioImage Suite, version 0.9.10), as previously reported [19]. Image activity in mCi/cc was then corrected by injected dose and animal body weight in grams (g) and displayed as standardized uptake value (SUV) for image quantification.

In order to appropriately visualize the spatial-temporal changes in gene expression over time, representative serial SPECT/CT images were semi-automatically registered using algorithms available in BioImage Suite and defined in the supplemental materials. Displayed representative SPECT/CT were created using AMIDE software (version 1.0.4) [20], with the display scale for each image being normalized to injected dose and body weight and was expressed as SUV.

Gamma Well Counting—The left and right GA muscles were harvested immediately following euthanasia in all animals to quantitate $^{99m}TcO_4^-$ activity by gamma well counting (Cobra Auto-Gamma, Perkin Elmer, Waltham, MA) using methods previously described [21]. In addition, endogenous NIS-expressing (salivary gland [submaxillary], stomach and thyroid) and non-endogenous NIS-expressing (liver, kidney, bladder, spleen, heart and blood) organs were also collected in a sub group of animals in blocking study (n=30) to confirm adequate NIS inhibition. Tissue activity was calculated as percentage of injected dose per gram of tissue (%ID/g).

Immunoblotting—Membrane proteins (20 μg) from a portion of harvested GA muscles were isolated and resolved by SDS-PAGE. Blots were probed with 4nM affinity-purified anti-human NIS antibody [22] followed by anti-rabbit HRP-conjugated secondary antibody (1:3,000; Jackson ImmunoResearch Laboratories, West Grove, PA) and were imaged and quantified as described in the supplemental material.

Immunofluorescence—Muscle tissue sections were incubated with primary antibodies against hNIS, the muscle specific, glucose transporter 4 (GLUT 4), and an endothelial marker (CD34) [23] and imaged by fluorescence microscopy using a Zeiss LSM 800 Airyscan confocal microscope, as described in the supplemental materials. eGFP expression was also visualized to co-validate AAV9-mediated gene expression and distribution, as the AAV9 vector also expressed eGFP.

Statistical Analysis—All statistical analyses were performed with Prism 8 (GraphPad Software, San Diego, CA, USA). A two-way analysis of variance (ANOVA) was used to examine the effect group, time (or ClO_4^-) and group * time (or ClO_4^-) on dependent variables of interest. Post hoc analyses were performed with a Sidak multiple comparison test. Pearson's correlations were used to determine the relationship between imaging and *ex*

vivo assays. In addition, correlations and Bland-Altman analyses were used to determine the relationship and agreement, respectively, between SUV values derived from manual segmented VOIs compared to VOIs derived from the U-net learning algorithm. All data are expressed as means ± SEM. The significance level was set *a priori* at $P < 0.05$.

Results

Validation of automated deep-learning image analysis approach

To assess the validity of our automated-segmentation approach, we first compared radiotracer uptake results from VOIs derived from the deep learning algorithm (n=16) to manually segmented VOIs that were not used for algorithm training purposes (n=16). As shown in Figure 3A, there was a near perfect relationship between SUV values derived from the deep learning algorithm compared to values derived from manual segmentation (r^2 =0.988, P<0.0001). In addition, Bland-Altman analysis showed good agreement between these two methods, with no bias and acceptable upper and lower limits (Figure 3B).

In Vivo Specificity of $^{99m}TcO_4^-$ uptake by NIS in the gastrocnemius

SPECT/CT imaging was performed 10 days post AAV9 injection to assess AAV9-mediated NIS expression in skeletal muscle in the presence or absence of surgically-induced hind-limb ischemia (HLI) and/or pharmacological desialylation with NA (Figure 4). $^{99m}TcO_4^-$ uptake by SUV was 2- to 3-fold higher in non-ischemic muscle injected with AAV9-hNIS alone than in either PBS-injected or non-injected control muscles (Figure 4A, 4C, and 4D). When mice were subjected to HLI, NA, or the combination of both treatments, $^{99m}TcO_4^-$ uptake was further elevated by 4- to 5-fold as compared to mice that received AAV9-hNIS alone (Figure 4A, 4C and 4D).

To ascertain the uptake specificity of $^{99m}TcO_4^-$ by NIS in skeletal muscle, mice received either $^{99m}TcO_4^-$ alone or $^{99m}TcO_4^-$ and ClO_4^-. ClO_4^- markedly reduced $^{99m}TcO_4^-$ uptake in ischemic and non-ischemic (with or without NA) skeletal muscle injected with AAV9-hNIS, and this difference reached significance in all groups (P<0.0001) except for the AVV9-hNIS alone group (Figure 4B–D). There were no significant differences in $^{99m}TcO_4^-$ uptake between groups following inhibition of NIS by ClO_4^-, demonstrating specificity of $^{99m}TcO_4^-$ uptake.

NIS protein was expressed in all AAV9-hNIS-treated skeletal muscles, but not in muscles from control mice (Figure 5A). Importantly, the magnitude and differences in NIS expression levels (Figure 5B) were consistent with $^{99m}TcO_4^-$ uptake as defined by both SPECT/CT and tissue well counting (Figure 4C, D). Moreover, *in vivo* $^{99m}TcO_4^-$ uptake was correlated to ex-vivo hNIS expression by Western blot analysis [Figure 5C; (r^2 =0.65, P<0.0001)

Serial detection of increased AAV9-mediated NIS functional expression over time

SPECT/CT imaging was also used to determine the spatiotemporal distribution of AAV9-driven NIS expression in skeletal muscle (Figure 6 A–C). As expected, $^{99m}TcO_4^-$ uptake in non-ischemic muscle injected with AAV9-hNIS alone was higher than in the controls,

reaching significance by day 10 (P<0.01) (Figure 6 B–C). Also, as expected, HLI and NA, and the combination of HLI + NA, increased the rate and magnitude of $^{99m}TcO_4^-$ uptake compared to AAV9-hNIS alone (Figure 6 B–C).

There was a significant stepwise increase in $^{99m}TcO_4^-$ uptake over time from day 3 to 10 and from day 10 to 14 in the NA, HLI, and NA + HLI groups [Figure 6 B,C (all P<0.001)]. In addition, $^{99m}TcO_4^-$ uptake was higher in these groups than in the AAV9-hNIS and control groups as early as day 7; this difference persisted up to day 28 (Figure 6 A–C).

Although skeletal muscle uptake of $^{99m}TcO_4^-$ was stable up to 28 days in the AAV9-hNIS alone group, we observed a subtle, non-significant decrease in radiotracer uptake from day 14 to 28 in the NA and HLI groups, and a significant decrease between these time points in the NA + HLI group (P<0.05). *Ex vivo* immunoblot analysis of GA muscle from animals representing each group, euthanized at different time points, showed similar temporal patterns of hNIS protein expression (Supplemental Figure 1).

We observed in the animals at day 28 of the time-course study that there was a very strong correlation between radiotracer retention values from *ex vivo* gamma well counting (% ID/gram of tissue) and *in vivo* SPECT radiotracer retention values (SUV) within VOIs derived from the deep learning algorithm (r^2 =0.9375, P<0.0001) (Figure 6 D).

Serial imaging also allowed for assessment of the regional distribution of the gene expression over time. Both coronal and transverse images of a representative animal show a clear increase of $^{99m}TcO_4^-$ uptake up to day 14 at the site of AAV9-hNIS delivery (Figure 6A). In addition, a decline of the SPECT signal was also evident at the injection site at day 28.

Biodistribution of $^{99m}TcO_4^-$ uptake

A subgroup of mice treated with (n=15) or without (n=15) ClO_4^- was used to determine the biodistribution of $^{99m}TcO_4^-$ uptake in other tissues. As expected, NIS-expressing tissues took up more $^{99m}TcO_4^-$ than non-NIS-expressing tissues (all P <0.001) (Supplemental Figure 2A, C). In addition, co-administration of ClO_4^- with $^{99m}TcO_4^-$ significantly reduced $^{99m}TcO_4^-$ uptake in organs that express NIS endogenously, whereas residual $^{99m}TcO_4^-$ uptake in non-NIS-expressing organs was not affected (Supplemental Figure 2B–C).

Skeletal muscle selectivity of AVV9-mediated expression of hNIS

Immunofluorescence (IF) staining of skeletal muscle tissue sections was used to determine the cellular localization and cell selectivity of AAV9-driven gene expression. As expected, NIS expression was localized to the sarcolemma, and the extent of NIS expression in the muscle samples from the various groups (Figure 7A) was similar to that determined by immunoblotting (Figure 5A). Tissue sections from ischemic and NA treated muscles showed similar hNIS expression patterns, whereas non-ischemic muscle injected with AAV9-hNIS alone displayed far fewer NIS-positive myofibers. Non-ischemic muscles untreated or injected with PBS displayed only background autofluorescence. The AAV9-hNIS vector contains the cDNA coding for eGFP, which enabled us to determine whether or not both

hNIS and eGFP were expressed in the same muscle fibers. Indeed, the expression patterns of hNIS and eGFP were co-localized to the same myofibers (Figure 7A).

To determine the cell selectivity of AVV9-mediated gene expression, we probed tissue sections for either muscle- (GLUT 4) or endothelial-specific markers (CD34) and used confocal microscopy to compare the expression of these markers to that of eGFP. Our results conclusively showed that eGFP co-localized with GLUT4, but not with CD34, confirming that gene expression is specific to skeletal muscle (Figure 7B, C).

Discussion

This study demonstrated that microSPECT/CT imaging of the hNIS reporter gene allows for accurate and sensitive non-invasive *in vivo* tracking and quantification of AAV9 delivery into skeletal muscle under non-ischemic and ischemic conditions. Specifically, we observed an increase in NIS-mediated $^{99m}TcO_4^-$ uptake along the site of vector delivery that was greater under ischemic conditions and when co-delivered with NA, an α-sialidase. Furthermore, there was a correlation between *in vivo* $^{99m}TcO_4^-$ uptake and levels of NIS expression, as demonstrated by immunoblot analysis. The imaging signal was specifically due to NIS, and not a result of changes in vascular permeability secondary to the experimental manipulation, since $^{99m}TcO_4^-$ uptake was competitively inhibited by ClO_4^-, a widely used NIS inhibitor. In addition, the accuracy of our *in vivo* quantification of $^{99m}TcO_4^-$ uptake from microSPECT/CT imaging was validated by *ex vivo* well counting of excised tissues.

The majority of preclinical gene therapy studies use optical imaging for *in vivo* monitoring of gene expression. However, light attenuation and scattering, especially at greater tissue depths, leads to degraded image detection sensitivity and resolution, which limits accurate quantification and precludes translation to large animals and humans. In this study, we provide an alternative and more translatable approach using microSPECT/CT imaging of NIS-mediated $^{99m}TcO_4^-$ uptake. This approach provides higher spatial resolution and tissue penetration than optical imaging, allowing for 3-dimensional tissue localization of AAV9-mediated gene transfer and accurate quantification of gene expression in skeletal muscle using a novel deep learning approach. In addition, the use of NIS as a reporter gene offers several advantages over other reporters. First, NIS activity reflects cell viability, as non-living cells are unable to transport any NIS substrate. Second, the NIS reporter gene provides high image detection sensitivity, given that NIS substrates are intracellularly accumulated rather than just bound to the cell surface, which is a saturable process. Third, NIS expression can be monitored with a variety of widely available NIS substrates, which makes it possible to use with both PET and SPECT. Finally, NIS is a human protein and will therefore not elicit an immune response[14]. Taken together, these properties make NIS a promising reporter gene for optimizing vector dosage and delivery in clinical studies of gene therapy in patients.

AAV9 has many features that make it an ideal vector for skeletal muscle gene transfer, since AAV9 transduces skeletal muscle more efficiently than other AAV serotypes, [10] and is able to provide sustained gene expression without provoking untoward immune responses [7].

Using optical imaging, previous groups have shown that AAV9-mediated skeletal muscle gene expression increases linearly over time and peaks between 14 and 56 days after injection, after which gene expression is stable for up to 9 months [10, 24]. Using microSPECT/CT imaging of NIS, we confirmed that AAV9-mediated skeletal muscle gene expression was stable for up to one month when delivered in non-ischemic muscle. However, there was a subtle decrease in AAV9 gene expression levels under ischemic conditions and with NA treatment to non-ischemic muscle, which was more pronounced when NA was delivered to ischemic muscle. The reason for this apparent decrease in AAV9-mediated gene expression is unclear, but it cannot be ruled out that a delayed immune response occurred in response to the high levels of AAV9 delivered along the needle track [15].

The high spatial resolution and image detection sensitivity afforded by the microSPECT/CT imaging of NIS activity enabled us to characterize for the first time *in vivo* the onset of AAV9-mediated NIS expression, showing that it steadily increases over the first two weeks at the site of vector delivery. We had anticipated these findings, as previous studies using microscopy show that direct vector injections produce a focal gene expression pattern with high gene expression in regions adjacent to the needle track that decrease exponentially with distance from the needle track [25]. In addition, the onset and peak of $^{99m}TcO_4^-$ uptake are in line with the previously reported *in vivo* kinetics of AAV9 mediated gene expression following injection[24].

AAV9 more efficiently transduces ischemic than non-ischemic skeletal muscle [8]. The mechanisms for increased AAV9 transduction under ischemic conditions into skeletal muscle have yet to be fully elucidated; however, one leading mechanism involves the desialylation of cell surface glycans leading to exposure of terminal *N*-linked ß-galactose residues [8], which are the primary receptors for AAV9 [26]. Thus, ischemia facilitates increased AAV9-cell binding and transduction. Along these lines, NA, a α-sialidase, has recently been used to increase AAV9- mediated transduction in non-ischemic mouse skeletal muscle [11]. We extended these findings, as we showed for the first time, an increase in NIS-mediated $^{99m}TcO_4^-$ uptake on microSPECT/CT with HLI and with NA treatment in non-ischemic skeletal muscle. The level of $^{99m}TcO_4^-$ uptake with NA was equivalent to that in ischemic skeletal muscle, while the delivery of NA to ischemic muscle did not further potentiate $^{99m}TcO_4^-$ uptake. This finding suggests that a biological desialylation 'ceiling' exists in skeletal muscle. Importantly, *in vivo* blocking studies with ClO_4^- demonstrated that $^{99m}TcO_4$ uptake was specifically mediated by NIS, rather than resulting from changes in vascular permeability associated with any of the treatments. Furthermore, the high image detection sensitivity provided by this nuclear imaging approach led to accurate detection of AAV9- driven gene expression, as evidenced by a good correlation with NIS protein expression.

The present study has some limitations that should be considered. First, we did not design the AAV9-hNIS vector to co-express a therapeutic gene with NIS, since our aim at this juncture was not to explore a novel therapy, but rather to provide a translatable approach for the serial *in vivo* evaluation of AAV9-gene expression. Therefore, we are unable to speculate on the relationship between NIS-mediated $^{99m}TcO_4^-$ uptake on SPECT/CT and a desired

therapeutic response. Notably, the viral dose used in these experiments is within the range of other reports that used AAV9 to deliver a transgene with a desired biological response when delivered directly into skeletal muscle in murine models of PAD [5, 6]. Second, we injected AAV9-hNIS intramuscularly in an effort to increase target-to-background AAV9-mediated NIS expression, which simplified our image analysis to one stationary region that was distant to high $^{99m}TcO_4^-$ accumulation areas (e.g., bladder, and endogenous NIS-expressing organs). Future studies using a systemic delivery approach or targeting organs with motion (e.g., heart) will likely need to employ correction for motion, scatter, and any other physical factors that degrade the quantitative accuracy of imaging, such as attenuation and partial volume errors.

Conclusion

SPECT/CT imaging of NIS-mediated $^{99m}TcO_4^-$ uptake allows for accurate and sensitive *in vivo* quantification of AVV9-mediated gene expression in skeletal muscle under non-ischemic and ischemic conditions. Importantly, this method was sensitive enough to detect low levels of AAV9-mediated NIS expression under non-ischemic conditions, and detected both regional and temporal changes in NIS expression. This imaging approach also demonstrated increased NIS expression in the presence of hind-limb ischemia, and in non-ischemic muscle with the co-administration of NA. These imaging techniques and findings can be directly translated to gene therapy studies in PAD patients and may also facilitate gene therapy applications in diseases of skeletal and cardiac muscle that are not associated with ischemia.

Supplementary Material

Refer to Web version on PubMed Central for supplementary material.

Acknowledgements

We gratefully acknowledge all of the staff of the Yale Translational Research Imaging Center, especially, Christi Hawley, Tsa Shelton and Xiangning Wang.

Funding sources:

This study was supported The NIH (Bethesda, MD) grants R01 HL11655–04 (B.H.A., B.A.F. and A.J.S.), T32 HL098069 (A.J.S.), S10 OD021845–01 (A.J.S.), R01 DK041544 (N.C.) and R24 MH114805 (X.P.)

References

1. Ouriel K Peripheral arterial disease. The Lancet. 2001;358:1257–1264
2. Benjamin EJ, Blaha MJ, Chiuve SE, Cushman M, Das SR, Deo R, de Ferranti SD, Floyd J, Fornage M, Gillespie C. Heart disease and stroke statistics—2017 update: A report from the american heart association. Circulation. 2017;135:e146–e603 [PubMed: 28122885]
3. Ghosh R, Walsh S, Tang T, Noorani A, Hayes P. Gene therapy as a novel therapeutic option in the treatment of peripheral vascular disease: Systematic review and meta-analysis. Int J Clin Pract. 2008;62:1383–1390 [PubMed: 18657197]
4. Jones WS, Annex BH. Growth factors for therapeutic angiogenesis in peripheral arterial disease. Curr Opin Cardiol. 2007;22:458–463 [PubMed: 17762548]

5. Boden J, Lassance-Soares RM, Wang H, Wei Y, Spiga MG, Adi J, Layman H, Yu H, Vazquez-Padron RI, Andreopoulos F, Webster KA. Vascular regeneration in ischemic hindlimb by adeno-associated virus expressing conditionally silenced vascular endothelial growth factor. J Am Heart Assoc.2016;5:1–19.
6. Chang DS, Su H, Tang GL, Brevetti LS, Sarkar R, Wang R, Kan YW, Messina LM. Adeno-associated viral vector-mediated gene transfer of vegf normalizes skeletal muscle oxygen tension and induces arteriogenesis in ischemic rat hindlimb. Mol Ther. 2003;7:44–51 [PubMed: 12573617]
7. Asokan A, Schaffer DV, Samulski RJ. The aav vector toolkit: Poised at the clinical crossroads. Mol Ther. 2012;20:699–708 [PubMed: 22273577]
8. Katwal AB, Konkalmatt PR, Piras BA, Hazarika S, Li SS, Lye RJ, Sanders JM, Ferrante EA, Yan Z, Annex BH. Adeno-associated virus serotype 9 efficiently targets ischemic skeletal muscle following systemic delivery. Gene Ther. 2013;20:930 [PubMed: 23535898]
9. Prasad K-MR, Xu Y, Yang Z, Acton ST, French BA. Robust cardiomyocyte-specific gene expression following systemic injection of aav: In vivo gene delivery follows a poisson distribution. Gene Ther. 2011;18:43–52. [PubMed: 20703310]
10. Zincarelli C, Soltys S, Rengo G, Rabinowitz JE. Analysis of aav serotypes 1–9 mediated gene expression and tropism in mice after systemic injection. Mol Ther. 2008;16:1073–1080 [PubMed: 18414476]
11. Zhu H, Wang T, John Lye R, French BA, Annex BH. Neuraminidase-mediated desialylation augments aav9-mediated gene expression in skeletal muscle. J Gene Med. 2018;20:e3049 [PubMed: 30101537]
12. Badr CE. Bioluminescence imaging: Basics and practical limitations. Methods Mol Biol. 2014;1098:1–18. [PubMed: 24166364]
13. Dai G, Levy O, Carrasco N. Cloning and characterization of the thyroid iodide transporter. Nature. 1996;379:458–460 [PubMed: 8559252]
14. Ravera S, Reyna-Neyra A, Ferrandino G, Amzel LM, Carrasco N. The sodium/iodide symporter (nis): Molecular physiology and preclinical and clinical applications. Annu Rev Physiol. 2017;79:261–289 [PubMed: 28192058]
15. Moulay G, Ohtani T, Ogut O, Guenzel A, Behfar A, Zakeri R, Haines P, Storlie J, Bowen L, Pham L. Cardiac aav9 gene delivery strategies in adult canines: Assessment by long-term serial spect imaging of sodium iodide symporter expression. Mol Ther. 2015;23:1211–1221 [PubMed: 25915925]
16. Dobrucki LW, Dione D, Kalinowski L, Dione D, Mendizabal M, Yu J, Papademetris X, Sessa WC, Sinusas AJ. Serial non-invasive targeted imaging of peripheral angiogenesis: Validation and application of a semi-automated quantitative approach. J Nucl Med. 2009;50:1356 [PubMed: 19617325]
17. Hedhli J, Slania SL, Płoska A, Czerwinski A, Konopka CJ, Wozniak M, Banach M, Dobrucki IT, Kalinowski L, Dobrucki LW. Evaluation of a dimeric-crgd peptide for targeted pet-ct imaging of peripheral angiogenesis in diabetic mice. Sci Rep. 2018;8:5401 [PubMed: 29599497]
18. Ronneberger O, Fischer P, Brox T. U-net: Convolutional networks for biomedical image segmentation. MICCAI. 2015:234–241
19. Suh JW, Scheinost D, Dione DP, Dobrucki LW, Sinusas AJ, Papademetris X. A non-rigid registration method for serial lower extremity hybrid spect/ct imaging. Medical image analysis. 2011;15:96–111 [PubMed: 20869902]
20. Loening AM, Gambhir SS. Amide: A free software tool for multimodality medical image analysis. Mol Imaging. 2003;2:131–137. [PubMed: 14649056]
21. Hua J, Dobrucki LW, Sadeghi MM, Zhang J, Bourke BN, Cavaliere P, Song J, Chow C, Jahanshad N, van Royen N. Noninvasive imaging of angiogenesis with a 99m tc-labeled peptide targeted at α v β 3 integrin after murine hindlimb ischemia. Circulation. 2005;111:3255–3260. [PubMed: 15956134]
22. Levy O, Dai G, Riedel C, Ginter CS, Paul EM, Lebowitz AN, Carrasco N. Characterization of the thyroid na+/i− symporter with an anti-cooh terminus antibody. Proc Natl Acad Sci USA. 1997;94:5568–5573 [PubMed: 9159113]

23. Muller AM, Hermanns MI, Skrzynski C, Nesslinger M, Muller KM, Kirkpatrick CJ. Expression of the endothelial markers pecam-1, vwf, and cd34 in vivo and in vitro. Exp Mol Pathol. 2002;72:221–229. [PubMed: 12009786]

24. Saqib A, Prasad K-MR, Katwal AB, Sanders JM, Lye RJ, French BA, Annex BH. Adeno-associated virus serotype 9-mediated overexpression of extracellular superoxide dismutase improves recovery from surgical hind-limb ischemia in balb/c mice. J Vasc Surg. 2011;54:810–818. [PubMed: 21723687]

25. French BA, Mazur W, Geske RS, Bolli R. Direct in vivo gene transfer into porcine myocardium using replication-deficient adenoviral vectors. Circulation. 1994;90:2414–2424. [PubMed: 7525108]

26. Shen S, Bryant KD, Brown SM, Randell SH, Asokan A. Terminal n-linked galactose is the primary receptor for adeno-associated virus 9. J Biol Chem. 2011;286:13532–13540. [PubMed: 21330365]

Clinical Perspective

Peripheral arterial disease (PAD) affects over 8 million Americans. PAD is more common and advances more quickly in patients with diabetes mellitus (DM) and involves both obstructive atherosclerosis of the large vessels and microvascular disease, which complicates the evaluation and treatment of PAD. Novel therapeutic approaches, such as gene delivery of angiogenic factors that stimulate the growth of new blood vessels in ischemic tissues, have been investigated using several delivery systems and therapeutic genes. The use of adeno-associated virus (AAV)–based vectors, which have low immunogenicity and provide for long term gene expression in muscle tissue has addressed some of the limitations in previous gene therapy clinical trials. In this study, incorporation of the sodium/iodide symporter (NIS) and SPECT/CT imaging of NIS-mediated $^{99m}TcO_4^-$ uptake allowed for accurate and sensitive *in vivo* quantification of AVV9-mediated gene expression in skeletal muscle. Importantly, SPECT imaging of NIS was sensitive enough to detect low levels of AAV9-mediated NIS expression under non-ischemic conditions, and detected both regional and temporal changes in NIS expression. This imaging approach also demonstrated increased NIS expression in the presence of hind-limb ischemia, and in non-ischemic muscle with the co-administration of the α-sialidase neuraminidase, which has been used as an adjuvant to increase AAV9-mediated gene expression. The use of the NIS reporter gene in combination with AAV9-mediated transduction can be directly translated to gene therapy studies in PAD patients and may also facilitate gene therapy applications in diseases of skeletal and cardiac muscle that are not associated with ischemia.

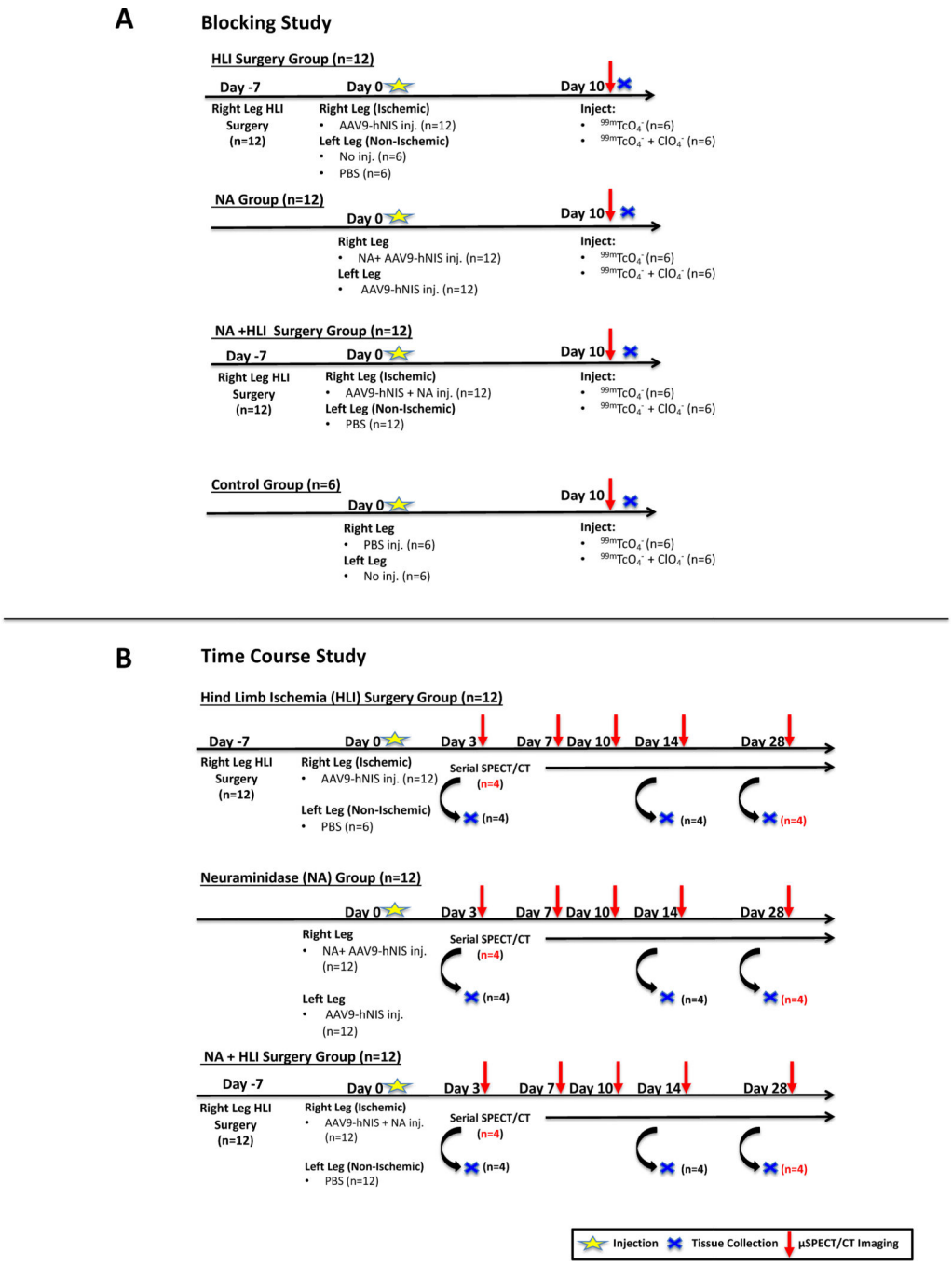

Figure 1: Schematic representation of study design and procedures.

Red numbers indicate animals with serial imaging. Red arrows indicate microSPECT/CT imaging. The blue X denotes tissue collection following euthanasia. AAV9= adeno-associated virus 9; hNIS=human sodium/ iodide symporter; HLI= Hind-limb ischemia; inj.= injection; PBS= Phosphate Buffered Saline; NA=Neuraminidase; γ=gamma; $^{99m}TcO_4^-$= pertechnetate; ClO4=perchlorate.

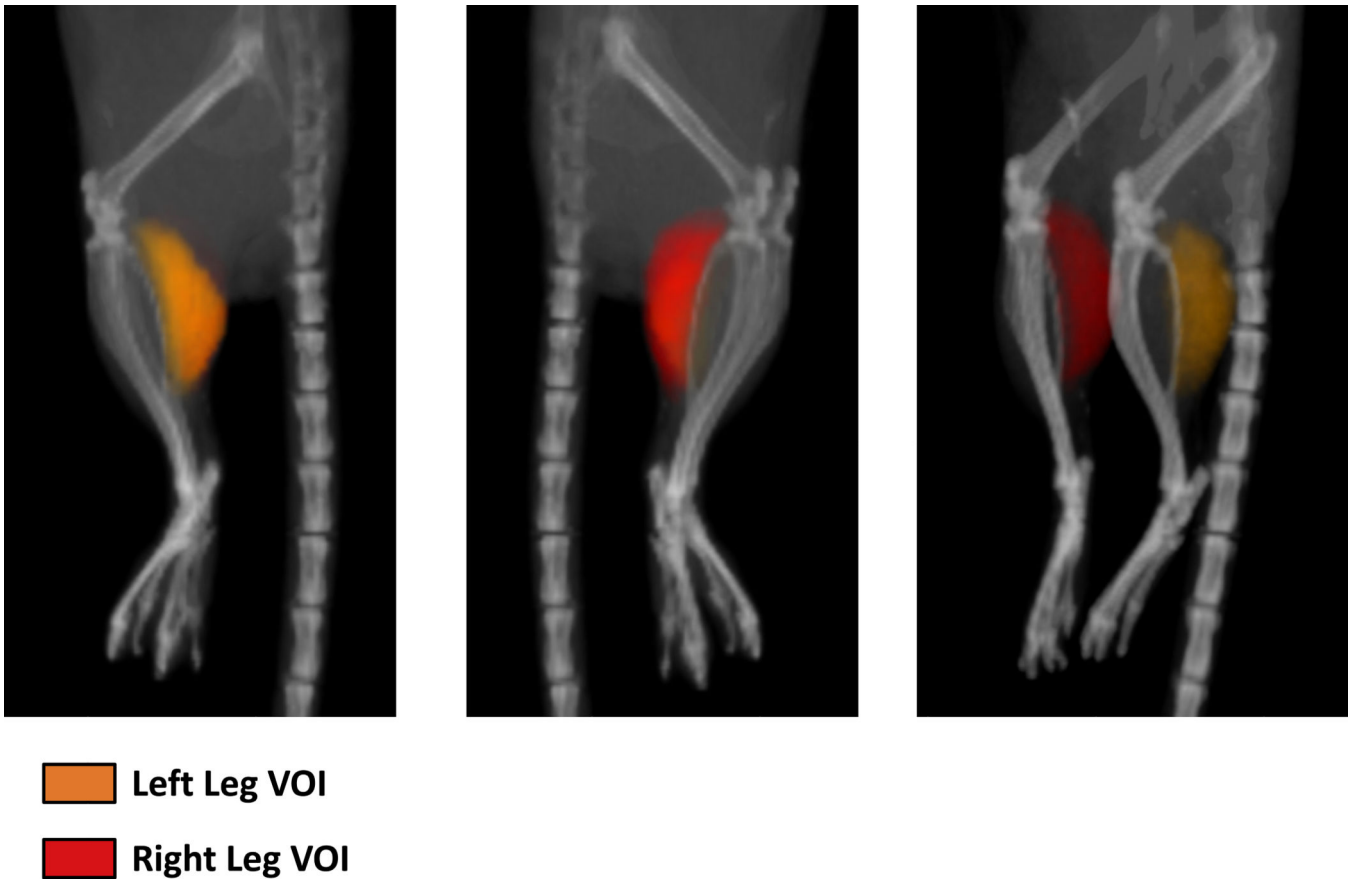

Figure 2:
Representative image of the volumes of interest (VOIs) of the right (red) and left (yellow) gastrocnemius muscles automatically generated on 3-dimensional micro-CT images (80 μm resolution) using a deep learning algorithm interfaced with BioImage Suite Software.

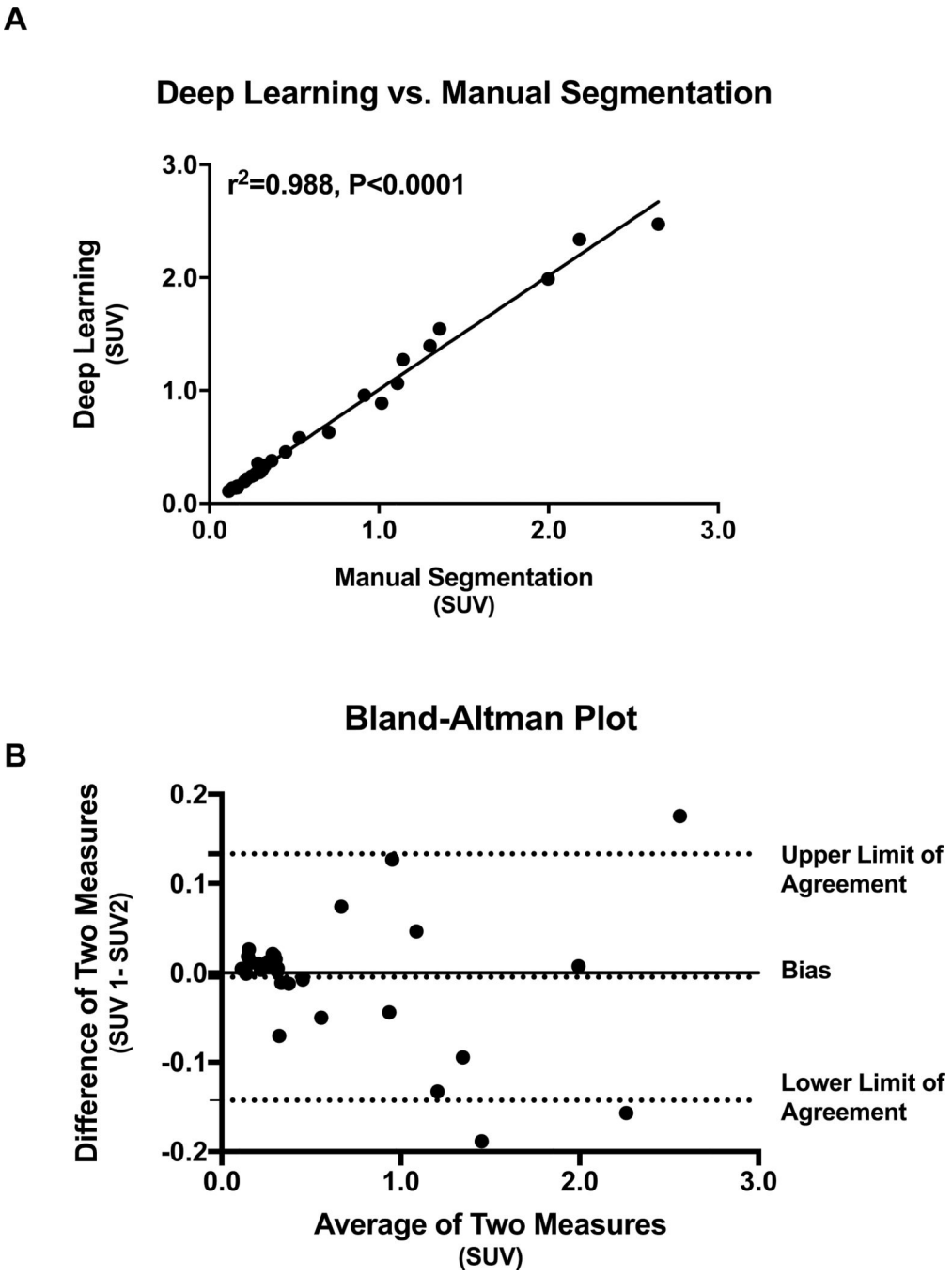

Figure 3: Validation of automated deep-learning image analysis approach.

A) Correlation between $^{99m}TcO_4^-$ uptake values using volumes of interest (VOIs) generated by deep learning compared to manual segmented VOIs. B) Bland-Altman Plot of the agreement between these two methods. %ID/g = % injected dose per gram of tissue; SUV= standardized uptake value.

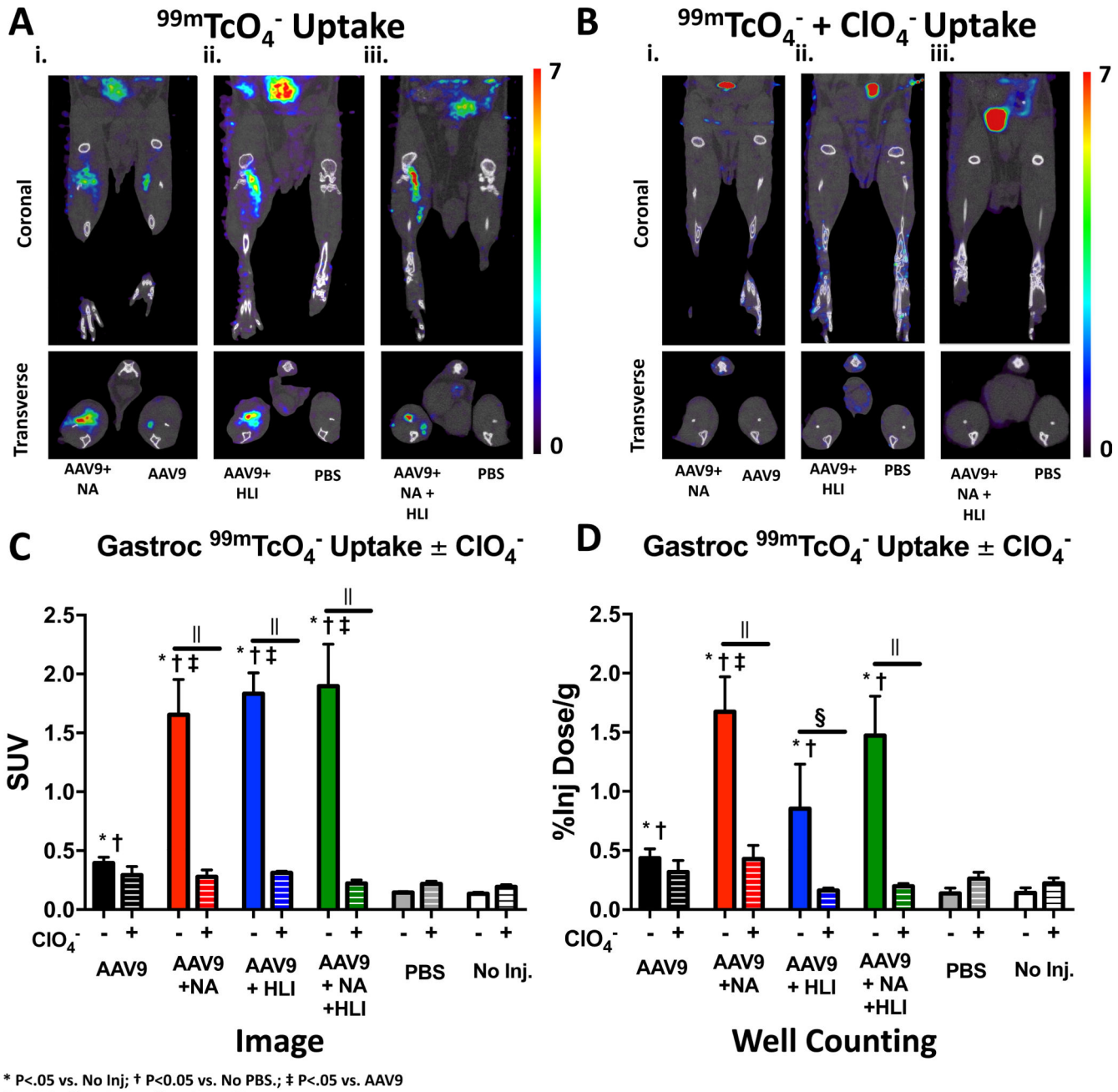

* P<.05 vs. No Inj; † P<0.05 vs. No PBS.; ‡ P<.05 vs. AAV9
§ P<0.05 $^{99m}TcO_4^-$ vs. $^{99m}TcO_4^-$ + ClO_4^-
|| P<0.0001 $^{99m}TcO_4^-$ vs. $^{99m}TcO_4^-$ + ClO_4^-

Figure 4: NIS-mediated $^{99m}TcO_4^-$ uptake in the gastrocnemius is inhibited by perchlorate (ClO_4^-).

A) Representative coronal and transverse microSPECT/CT images of $^{99m}TcO_4^-$ uptake on day 10 following NA and AAV9-hNIS co-injection into the right hind-limb and injection of AAV9-hNIS alone into the left leg (i); a mouse injected with AAV9-hNIS into ischemic right hind-limb and injected with phosphate buffered saline (PBS) in left hind-limb (ii.); and a mouse injected with AAV9-hNIS + NA into ischemic right hind-limb and injected with phosphate buffered saline (PBS) in left hind-limb (iii.). **B)** Same as A, except that $^{99m}TcO_4^-$

was co-administered with ClO_4^-. **C)** Quantitative analysis of differences in gastrocnemius $^{99m}TcO_4^-$ uptake derived from microSPECT/CT images in mice without (−) and with (+) co-administration of ClO_4^-. D) Quantitative analysis of differences in gastrocnemius $^{99m}TcO_4^-$ uptake in mice without (−) and with (+) co-administration of ClO_4^- derived from *ex vivo* gamma well counting. Image quantification and display are the same as in Figure 3. For gamma well counting, tissue activity is displayed as the ratio of gastrocnemius $^{99m}TcO_4^-$ activity (% ID/g). * = $P < 0.05$ vs. no injection, †= $P< 0.05$ vs. PBS injection and ‡= $P<0.05$ vs. AA9-hNIS injection. § =$P<0.05$ within group difference between mean$^{99m}TcO_4^-$ gastrocnemius uptake with and without ClO_4^-; || =$P<0.0001$ within group difference between mean$^{99m}TcO_4^-$ gastrocnemius uptake with and without ClO_4^-.

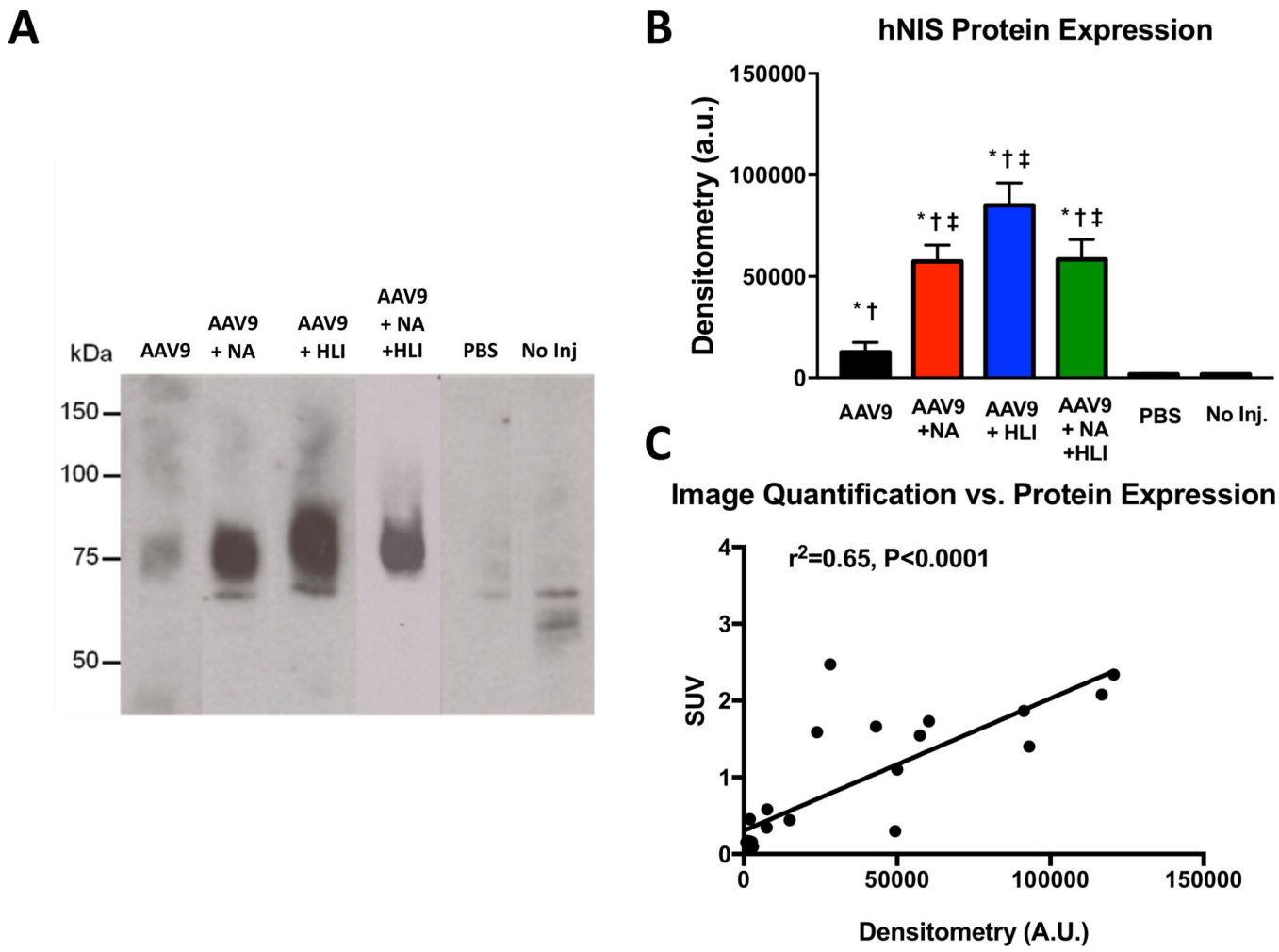

Figure 5: Ischemia and neuraminidase treatments promote AAV9-driven hNIS expression.

A) Representative immunoblot of NIS protein expression. **B)** Densitometric quantitation of hNIS expression from all 84 muscle samples analyzed. **C)** Correlation between $^{99m}TcO_4^-$ on SPECT imaging and NIS protein expression from immunoblot on day 10. * = P < 0.05 vs. no injection, † = P< 0.05 vs. PBS injection and ‡ = P<0.05 vs. AA9-hNIS injection. A.U.= arbitrary units.

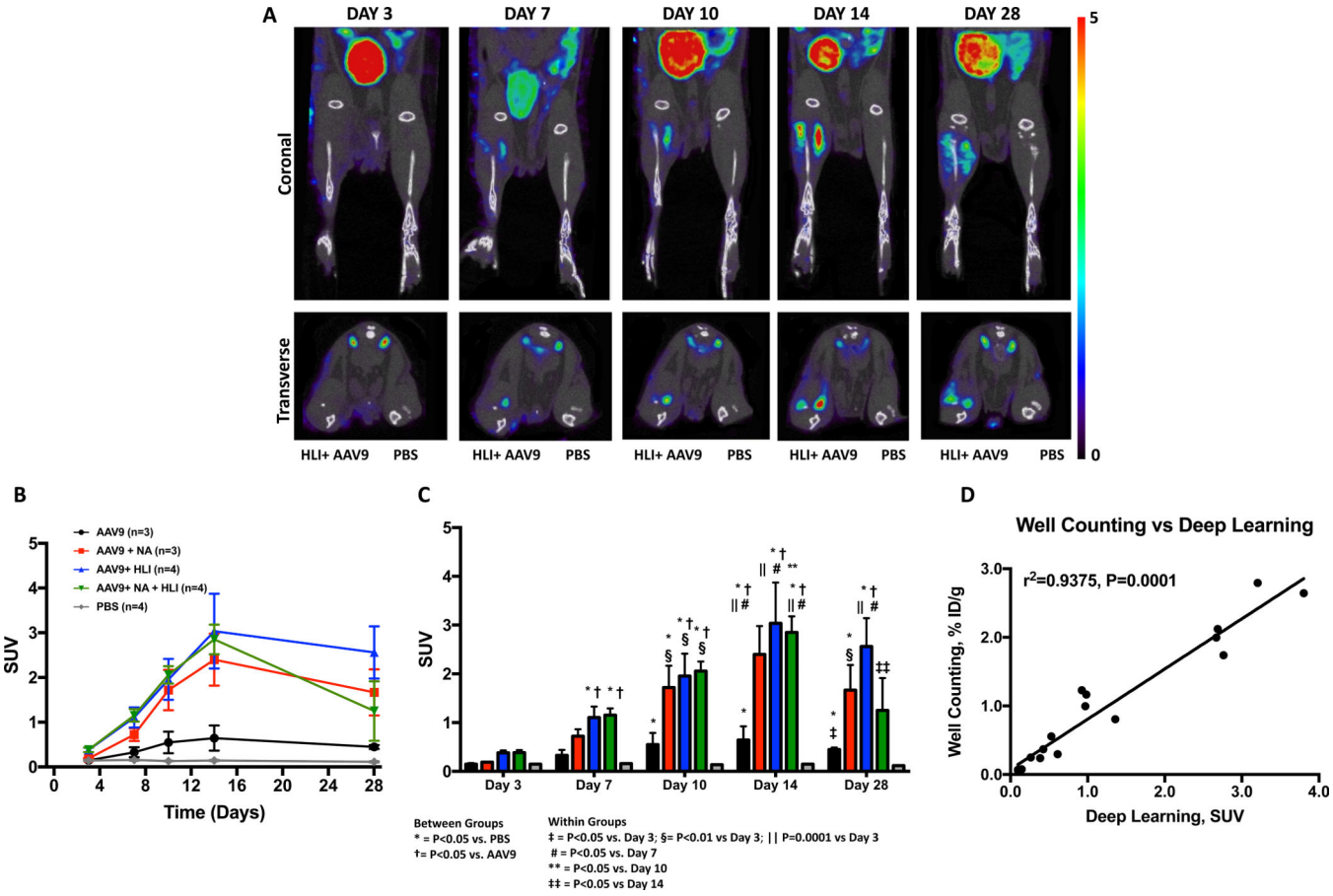

Figure 6: Serial detection of increased AAV9-driven NIS expression over time using microSPECT/CT.

A) Representative coronal and transverse microSPECT/CT images of $^{99m}TcO_4^-$ uptake in gastrocnemius muscles on days 3, 7, 10, 14 and 28 following intramuscular injection of AAV9-hNIS in a mouse that underwent unilateral surgical ischemia of the right hind-limb and had PBS delivered into the left hind-limb. Each representative image's display scale was normalized to the injected dose and body weight and displayed as SUV. **B)** Time course **C)** Quantitative analysis of gastrocnemius $^{99m}TcO_4^-$ uptake derived from microSPECT/CT images, and **D)** Correlation between $^{99m}TcO_4^-$ uptake values using VOIs generated by the deep learning algorithm compared to *ex vivo* $^{99m}TcO_4^-$ uptake values from tissue well counting. For image quantification, image activity in mCi/cc was corrected for injected dose and animal body weight, and also displayed as, SUV. * = P<0.05 vs. PBS; † = P<0.05 vs. AAV9-hNIS; ‡ P<0.05 vs. day, § P<0.01 vs. day 3, || P=0.0001 vs. day 3; # = P < 0.05 vs. day 7; ** = P< 0.05 vs. day 10 and ‡‡= P<0.05 vs. day 14.

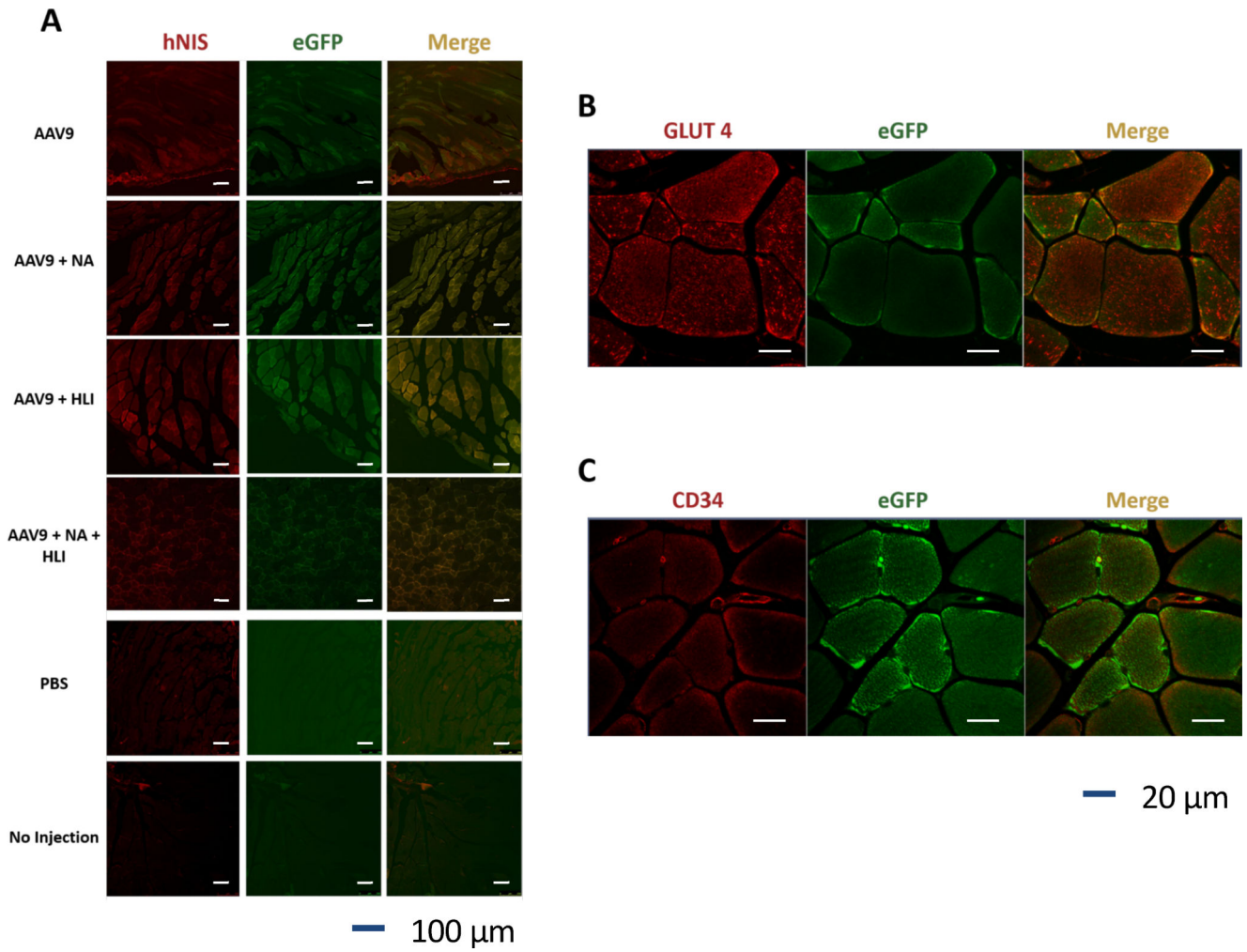

Figure 7: Representative immunofluorescence images of the cellular distribution of hNIS and eGFP expression.

A) hNIS expression and distribution (red fluorescence) and enhanced green fluorescent protein (eGFP) expression and distribution (green fluorescence). Merged hNIS and eGFP fluorescent signals (yellow) indicating co-localization. Scale bar = 100 µm **B)** glucose transporter (GLUT4, red) and eGFP expression. C) CD34 (red) and eGFP expression. Merged GLUT4 and eGFP fluorescent signals (yellow) indicating co-localization. Scale bar = 20 µm